

The QUEST-La Silla AGN Variability Survey: selection of AGN candidates through optical variability

P. SÁNCHEZ-SÁEZ,^{1,2} P. LIRA,¹ R. CARTIER,³ N. MIRANDA,⁴ AND ET AL.

¹*Departamento de Astronomía, Universidad de Chile, Casilla 36D, Santiago, Chile*

²*European Southern Observatory, Casilla 19001, Santiago 19, Chile*

³*Cerro Tololo Inter-American Observatory, National Optical Astronomy Observatory, Casilla 603, La Serena, Chile*

⁴*Institut für Informatik, Humboldt-Universität zu Berlin*

ABSTRACT

We present our variability-based active galactic nuclei (AGN) selection technique. We used data from the QUEST-La Silla AGN variability survey to construct light curves for 208,583 sources. We used different features to characterize the variability of our sources, and we implemented a Random Forest (RF) algorithm to classify our objects as either AGN or non-AGN according to their variability features and optical colors. We tested two classifiers, one that includes only variability features (RF1), and another one that includes variability features and $r - i$ and $i - z$ colors (RF2). We trained our classifiers using a sample of spectroscopically confirmed AGN and stars. We obtained a sample of high probability candidates for each classifier, with 5,941 sources for RF1 and 5,252 sources for RF2. We divided each sample according to their $g - r$ colors, defining a blue ($g - r \leq 0.6$) and a red sample ($g - r > 0.6$). We confirmed the nature of some of our candidates using ancillary data, and we found that a 61% of the blue candidates of RF1 and RF2 are known from the literature, but less than the 10% of the red candidates of RF1 and RF2 have been previously confirmed. In order to test the efficiency of our technique we performed a spectroscopic follow up campaign, observing 54 candidates, and we confirmed the AGN nature of 44 sources (81% of efficiency). From the campaign we concluded that the best classifier is RF2, since it provides the purest sample of AGN candidates. For the RF2 classifier, we confirmed 100% and 80% of the blue and red candidates respectively. The most interesting confirmed sources belong to the red sample, with 5 BAL-QSO, 8 LLAGN, and 5 high redshift AGN.

Keywords: galaxies: active - methods: statistical - surveys

1. INTRODUCTION

Active galactic nuclei (AGN) are one of the most energetic phenomena in the universe and are characterized by their time-variable emission in every waveband in which they have been studied. Variability studies are fundamental to understanding the extreme physical conditions of accretion disks near super massive black holes (SMBH). AGN variability seems to be well described as a stochastic process (Kelly et al. 2009, 2014), with characteristic time-scales ranging from days to years.

AGN are commonly classified in the optical range by the presence or absence of broad permitted emission lines ($\text{FWHM} > 2000 \text{ km s}^{-1}$), into broad-line (BL) AGN (or type 1) and narrow-line (NL) AGN (or type 2), respectively. The unified model is one of the most successful approaches to explain this dichotomy. It postulates that a dusty torus around the central engine is responsible for the different classes of AGN, which occur when we observe the source at different angles (Antonucci & Miller 1985). The most promising models

include a clumpy torus and disk winds (see Netzer 2015 and references therein), as they would explain the torus spectral energy distribution (SED) observed in the near-infrared (NIR) and mid-infrared (MIR) bands and the existence of at least some “changing look” AGN (e.g. LaMassa et al. 2015).

The Large Synoptic Survey Telescope (LSST; Ivezić et al. 2008) will revolutionize time-domain astronomy, providing for the first time the opportunity to study variable objects for a long period of time (~ 10 years), at very low magnitudes ($r \sim 24.5$ for the single images), and with a large total covered area ($25,000 \text{ deg}^2$). Simulations performed by the LSST AGN Science Collaboration predict a detection of over 10^7 AGN to beyond $m \sim 24$ (LSST Science Collaboration et al. 2009). This is a huge improvement in the number of sources available for variability analysis since current studies typically reach a limiting magnitude of $m \sim 21$ with between 10 and 10^5 sources. Given the importance of variability and the large number of objects expected it is critical

to characterize AGN variability and define reliable selection criteria before LSST’s first observations.

Traditionally, the AGN selection follows the philosophy of finding regions in an UV/optical color-color space in which AGN can be cleanly separated from stars (e.g. Richards et al. 2002, 2009; Ross et al. 2012). However, some AGN populations are known for having colors that fall outside the region occupied typically by AGN, mimicking those of stars, such as broad absorption line quasars (BAL QSO) and high redshift quasars (high- z QSO) (Butler & Bloom 2011; Palanque-Delabrouille et al. 2011), or low luminosities AGN (LLAGN), whose colors can be highly contaminated by the emission from the host galaxy. Therefore, we need alternative methods to identify AGN candidates with the upcoming time domain surveys. Promising selection methods involve the use of variability techniques.

Butler & Bloom (2011) implemented a variability-based selection algorithm to classify high redshift quasars in the Sloan Digital Sky Survey (SDSS; York et al. 2000) Stripe 82 field. They used damp random walk modelling (Kelly et al. 2009) to separate sources showing stochastic (or quasar-like) variability from those with temporally uncorrelated variability. Particularly, they targeted sources with redshifts in the range $2.5 \leq z \leq 3$, where color-based selection of AGN is quite difficult. Palanque-Delabrouille et al. (2011) used the variability structure function (e.g Schmidt et al. 2010) to separate quasars, variable stars, and non-variable stars, in the SDSS Stripe 82 data. They implemented a neural network algorithm that separates the classes considering their structure function parameters. A similar technique has been used by the SDSS IV *the extended Baryon Oscillation Spectroscopic Survey* (eBOSS) team to select quasar candidates with $z > 2.1$ by variability (Myers et al. 2015). More recently, Tie et al. (2017) used data from the supernova fields of the Dark Energy Survey (DES; Abbott et al. 2018) to select quasars by combining color and variability selection methods. All these previous works have shown the capability of selecting AGN candidates through variability analyses, demonstrating that variability-based techniques can increase considerably the number of AGN candidates in the redshift range where the colors of stars are similar to those of AGN.

In this paper we present our variability-based technique to select AGN candidates using data from the QUEST-La Silla AGN variability survey (Cartier et al. 2015). Variability features, like the structure function, have been used to characterize the variable sources. We then used a Random Forest algorithm to classify our objects as either AGN or non-AGN. We tested two clas-

sifiers, one that includes only variability features, and another one that includes colors and variability features. For some of our candidates we have performed spectroscopic follow ups. Four of the fields observed by the QUEST-La Silla AGN variability survey correspond to the LSST Deep Drilling Fields (DDF), and the expected cadence of the DDF will be similar to the one used by the QUEST-La Silla AGN variability survey (but covering 10 years)¹. Thus, our work is a perfect pilot study for the selection of AGN with LSST.

The paper is organized as follows. In Section 2 we describe the QUEST-La Silla AGN variability survey, and the light curve construction procedure. In Section 3 we describe the Random Forest algorithm, the variability features, and the labeled set used for the selection. We also discuss the performance of our Random Forest classifiers, and we provide the list of selected candidates. In Section 4 we provide the results on confirming the nature of some of our candidates by using public data and spectroscopic follow ups. In Section 5, we provide a comparison of our results with previous works. Finally, in Section 6 we summarize the main results.

2. DATA

2.1. The QUEST-La Silla AGN variability survey

Between 2010 and 2015 we carried out “The QUEST-La Silla AGN variability survey” (hereafter QUEST-La Silla), using the wide-field QUEST camera on the 1m ESO-Schmidt telescope at La Silla Observatory (Cartier et al. 2015). Our survey includes the COSMOS, ECDF-S, ELAIS-S1, XMM-LSS and Stripe 82 fields. These are some of the most intensively observed regions in the southern sky. Our QUEST fields are much larger than just COSMOS, ELAIS-S1, etc., even though we use the same names for them, with a surveyed area of $\sim 7 \text{ deg}^2$ per field. One of the advantages of our survey over other surveys was the very intense monitoring, observing the fields every possible night. Individual images reached a limiting magnitude between $r \sim 20.5$ and $r \sim 21.5$ mag for a exposure time of 60 seconds or 180 seconds, respectively.

The aims of our survey are: 1) to test and improve variability selection methods of AGN, and find AGN populations missed by other optical selection techniques (Schmidt et al. 2010; Butler & Bloom 2011; Palanque-Delabrouille et al. 2011); 2) to obtain a large number of well-sampled light curves, covering time-scales ranging from days to years; 3) to study the link between the variability properties (e.g., characteristic time-scales

¹ <https://www.lsst.org/scientists/survey-design/ddf>

and amplitudes of variation) with physical parameters of the system (e.g., black-hole mass, luminosity, and Eddington ratio).

Cartier et al. (2015) presented the technical description of the survey, the full characterisation of the QUEST camera, and a study of the relation of variability with multi-wavelength properties of X-ray selected AGN in the COSMOS field. In Sánchez-Sáez et al. (2018) we performed a statistical analysis of the connection between AGN variability and physical properties of the central SMBH, where we found that the amplitude of the variability (A) depends solely on the rest-frame emission wavelength (λ_{rest}) and the Eddington ratio, where A anticorrelates with both λ_{rest} and L/L_{Edd} .

2.2. Light curve construction

We reduced the data from the QUEST–La Silla using our own customized pipeline, following the same procedure described by Cartier et al. (2015), which includes dark subtraction, flat-fielding, and astrometric and photometric calibration. To calibrate the photometry, we used public photometric SDSS catalogs (Gunn et al. 1998; Doi et al. 2010) for the COSMOS, Stripe 82 and XMM–LSS fields, and public catalogs from the first year of DES (Abbott et al. 2018) for the ELAIS–S1 and ECDF–S fields. We performed aperture photometry using SExtractor (Bertin & Arnouts 1996), with the same optimal aperture found by Cartier et al. (2015) for the QUEST camera ($\sim 6''.18$). We then constructed light curves for all the sources from the SDSS and DES catalogs with detections in the QUEST–La Silla data, using the same methodology as in Cartier et al. (2015). From the SDSS catalog, we could obtain photometry of every source in the COSMOS, XMM–LSS, and Stripe 82 fields in the u , g , r , i , and z bands, and from the DES catalog we obtained photometry in the g , r , i , and z bands for the ELAIS–S1 and ECDF–S fields.

We decided to bin our light curves every three days, in order to reduce the noise in our light curves, produced by changes in atmospheric conditions, the relatively low quality of the QUEST camera, among other factors. In this work, we excluded the Stripe 82 field, since it is a crowded field, and requires point spread function (PSF) photometry. We generated a total of 277,629 light curves for sources located in the COSMOS, ECDF–S, ELAIS–S1, and XMM–LSS fields. In order to have statistically significant variability features of the sources, we decided to include in our analysis only those light curves with at least 40 epochs and a length greater than or equal to 200 days, after the three days binning was applied to the original light curves (hereafter well sampled light curves). There are 208,583 well

Table 1. Number of light curves per field.

Field	total light curves	well sampled light curves
COSMOS	68,514	45,323
XMM–LSS	104,962	82,697
Elais–S1	49,504	38,106
ECDF–S	54,649	42,457
Total	277,626	208,583

sampled light curves in the four fields. In average the well sampled light curves have 120 ± 48 epochs and a total length of 1306 ± 254 days. In Table 1 we summarize the total number of light curves and the number of well sampled light curves in each field.

3. SELECTION OF AGN CANDIDATES

We developed a variability–based AGN selection technique to find AGN populations missed by other optical selection methods. We implemented a supervised automatic classification using a Random Forest algorithm (RF; Breiman 2001) to classify our 208,583 objects with well sampled light curves as either AGN or non-AGN according to their variability features. We tested two classifiers, one that includes only variability features, and one that includes optical colors and variability features. In the following sections we describe the selection methodology, the features used in our analysis, and the results of the classification for sources from the QUEST–La Silla survey.

3.1. Random Forests

A type of learning algorithm that has been particularly effective in various applications are the so-called algorithms of ensemble learning. The idea of these algorithms is to add the results in the work of learning (or classification) of a large number of very simple models on subsets of the training data. The RF algorithm performs this by using simple models of decision trees. A decision tree is a hierarchical structure that performs successive partitions on the data, each of them according to a certain criteria, such as a cut-off value in one of the descriptors or features. In this way, the data is divided into smaller and smaller subsets as the tree goes deeper, until it reaches the leaves of the tree. Each of these leaves is associated with a single class, and therefore the elements that falls on the leaves corresponding to a particular class are those that will be classified as belonging to that class.

A RF algorithm constructs a large number of decision trees from random sub-sets of a training set. Each of

these classifiers then assigns a class to a certain input element. The final classification function of the algorithm ponders each of these results according to the size of the sub-set used by each tree, and generates an average score; which can then be interpreted as the probability that the input element belongs to a certain class (P_{RF}).

For the selection of AGN candidates we used the *scikit-learn*² Python package implementation of RF. We performed an hyperparameter selection procedure in order to obtain the optimal values for the RF classifier, by means of a cross-validated randomized search procedure and using the “accuracy” (see its definition in Section 3.4) as the target score to optimize. The parameters considered in this randomized search includes the number of trees in the forest, and the number of features to consider when looking for the best split. In order to take into account the class imbalance in the classification process, we initialized the class weight hyperparameter as “*balanced_subsample*”

The variability features used by the RF classifier are described in the following section (3.2), and are listed in Table 2. We trained the RF classifier using a labeled set of AGN and stars with spectroscopic classification from SDSS and with detections in the QUEST–La Silla survey (see Section 3.3). During the RF classifier training, we used the 30% of the labeled set as a test set, and a 70% of the labeled set as a training set. We then applied the obtained RF classifier to our unlabeled set, composed by our 208,583 sources with QUEST–La Silla light curves, to classify them as either AGN or non-AGN. As a result, we obtain a predicted class and the predicted class probability (P_{RF}) associated to each source of the unlabeled set.

3.2. Variability features

In order to have a complete description of the variability of our sources, we used several variability features. Following the same approach of Sánchez et al. (2017) and Sánchez-Sáez et al. (2018), we used two parameters related to the amplitude of the variability, P_{var} and the excess variance (σ_{rms}), and one method related to the structure of the variability, the structure function (SF).

In particular, P_{var} (see Sánchez et al. 2017 and references therein) corresponds to the probability that the source is intrinsically variable, it considers the χ^2 of the light curve, and calculates the probability $P_{\text{var}} = P(\chi^2)$ that a χ^2 lower or equal to the observed value could occur by chance for an intrinsically non-variable source.

σ_{rms} is a measure of the intrinsic variability amplitude (see Sánchez et al. 2017 and references therein), and it is calculated as $\sigma_{\text{rms}}^2 = (\sigma_{LC}^2 - \bar{\sigma}_m^2) / \bar{m}^2$, where σ_{LC} is the standard deviation of the light curve, $\bar{\sigma}_m$ is the mean photometric error, and \bar{m} is the mean magnitude.

The SF (e.g. Schmidt et al. 2010) is a measure of the amplitude of the variability as a function of the time lapse between compared observations (τ), and it can be modelled as a power law: $\text{SF}(\tau) = A_{\text{SF}} \left(\frac{\tau}{1\text{yr}} \right)^{\gamma_{\text{SF}}}$, where A_{SF} corresponds to the amplitude of the variability at 1 year, and γ_{SF} is the logarithmic gradient of this change in magnitude.

We also used some variability features from the Feature Analysis for Time Series (FATS; Nun et al. 2015) Python package, related with the amplitude of the variability (e.g. the mean variance and the percent amplitude) and the structure of the light curve (e.g. the linear trend and the auto-correlation function length), as well as the period of the Lomb-Scargle periodogram (VanderPlas 2018), derived by using the AstroML module for Python (VanderPlas et al. 2012). A list of all the variability features used in this work is shown in Table 2, together with a brief description of each feature and its reference.

3.3. Labeled set

Three of our fields (COSMOS, Stripe 82, and XMM–LSS) have spectroscopic information from SDSS. We selected a sample of 2,405 AGN and 2,608 stars with both SDSS spectral classification from the the SDSS-DR14 database (Abolfathi et al. 2018), and well sampled light curves from QUEST–La Silla, as our labeled set for the RF classifier training. As mentioned in Section 3.1, 30% of the labeled set was used as a test set and 70% as training set for the RF modelling. Figure 1 provides examples of QUEST–La Silla light curves for 4 sources of the labeled set.

In Figure 2 we show three color–color diagrams of the labeled set: $u - g$ versus $g - r$, $g - r$ vs $r - i$, and $r - i$ vs $i - z$. It can be seen that stars and AGN in general occupy well defined regions in the color–color spaces, this is expected, because the techniques used to select stars and AGN (e.g. Richards et al. 2002). In general, most of the stars are located in a region of the color–color space called stellar locus (e.g. Covey et al. 2007; Sesar et al. 2007). Since stellar colors become monotonically redder as the effective temperature decreases (Covey et al. 2007), we normally observe a high concentration of cold stars in a region around $g - r \sim 1.5$, with $r - i \gtrsim 0.8$. Moreover, extragalactic sources are normally located in regions of the color–color space with $r - i \lesssim 1.5$ and $i - z \lesssim 1.5$ (e.g. Rahman et al. 2016),

² <http://scikit-learn.org/stable/modules/generated/sklearn.ensemble.RandomForestClassifier.html>

Table 2. List of features.

Feature	Description	Reference
P_{var}	Probability that the source is intrinsically variable	McLaughlin et al. (1996)
σ_{rms}	Measure of the intrinsic variability amplitude.	Allevato et al. (2013)
A_{SF}	Amplitude of the variability at 1 year, derived from the SF	Schmidt et al. (2010)
γ_{SF}	Logarithmic gradient of the change in magnitude, derived from the SF	Schmidt et al. (2010)
Std*	Standard deviation of the light curve (σ_{LC})	Nun et al. (2015)
Meanvariance*	Ratio of the standard deviation to the mean magnitude (σ_{LC}/\bar{m})	Nun et al. (2015)
MedianBRP*	Fraction of photometric points within amplitude/10 of the median magnitude	Richards et al. (2011)
Autocor-length*	Lag value where the autocorrelation becomes smaller than e^{-1}	Kim et al. (2011)
StetsonK*	A robust kurtosis measure	Kim et al. (2011)
η^{e*}	Ratio of the mean of the square of successive differences to the variance of data points	Kim et al. (2014)
PercentAmp*	Largest percentage difference between either the max or min magnitude and the median	Richards et al. (2011)
Con*	number of three consecutive data points that are brighter or fainter than $2\sigma_{LC}$	Kim et al. (2011)
LinearTrend*	Slope of a linear fit to the light curve	Richards et al. (2011)
Beyond1Std*	Percentage of points beyond one σ_{LC} from the mean	Richards et al. (2011)
Q31*	Difference between the third quartile and the first quartile of a light curve	Kim et al. (2014)
PeriodLS	Period from the Lomb-Scargle periodogram	VanderPlas (2018)

Note. (*) Features from FATS

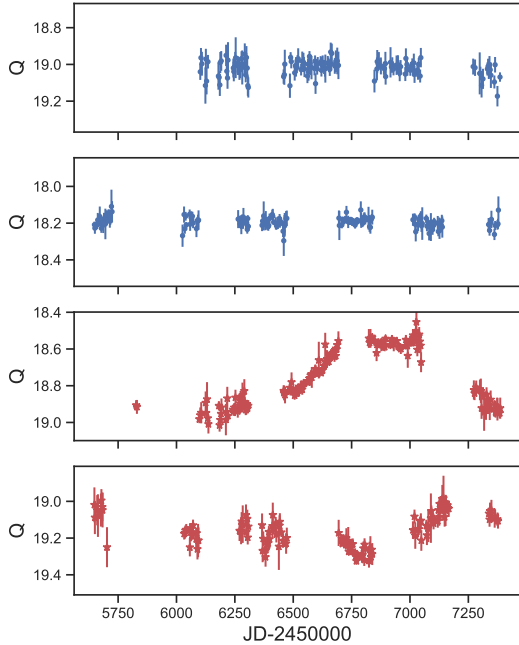


Figure 1. Example of four light curves from the QUEST–La Silla labeled set: two stars (blue dots) and two AGN (red stars).

since their integrated emission have a very low contribution from cold stars. In Figure 2 we can see that AGN in the labeled set occupy different positions of the $u - g$ vs $g - r$ space, however, in the $r - i$ vs $i - z$ space, they are concentrated in a particular area around $r - i \sim 0$ and $i - z \sim 0$. Therefore we can use the $r - i$ and $i - z$ colors to separate cold stars and extragalactic sources. We can also see from the figure that most of the AGN are concentrated in a region with $g - r \leq 0.6$.

3.4. Performance of the Random Forest classifier

We tested two different RF classifiers, the first one includes only variability features (hereafter RF1), and the second one includes variability features and the $r - i$ and $i - z$ colors (hereafter RF2). We only include the $r - i$ and $i - z$ colors, because they can easily separate cold stars and extragalactic sources. Besides, AGN in the labeled set occupy different positions in the $u - g$ vs $g - r$ diagram, thus, in order to avoid a selection biased by typical type 1 AGN, we exclude these colors.

3.4.1. Classification considering variability features

Our first RF classifier (RF1) includes only variability features. After the training of RF1 we tested its performance by using the confusion matrix, which is shown in Figure 3. It can be seen that AGN (true positives) are in general well classified, and also that the fraction of stars classified as AGN (false positives) is very low.

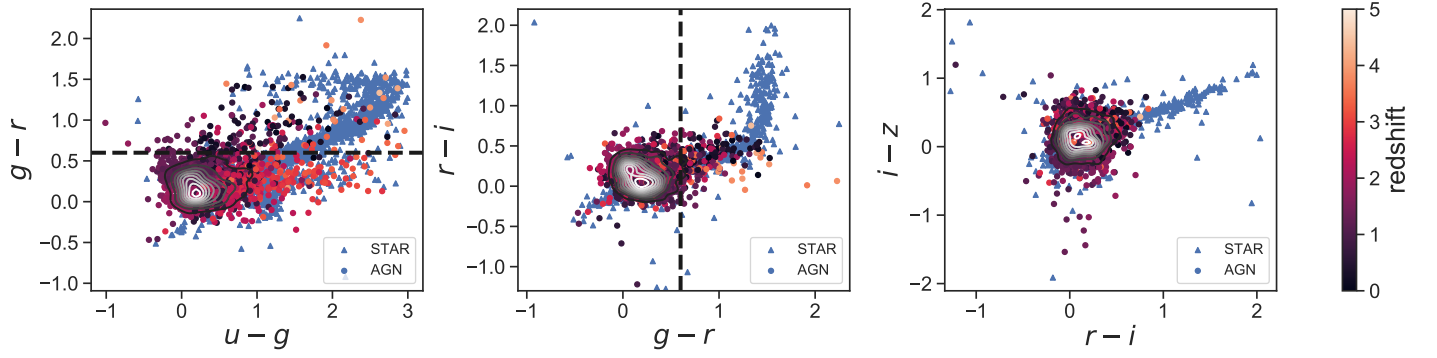


Figure 2. Color-color diagrams of the labeled set. In the left panel we show $u - g$ versus $g - r$, in the middle panel $g - r$ vs $r - i$, and in the right panel $r - i$ vs $i - z$. The stars are represented by blue triangles, and the AGN are represented by circles whose colors depend on the redshift of every source. The contour plots show the distribution of AGN. The black dashed line shows the position where $g - r = 0.6$.

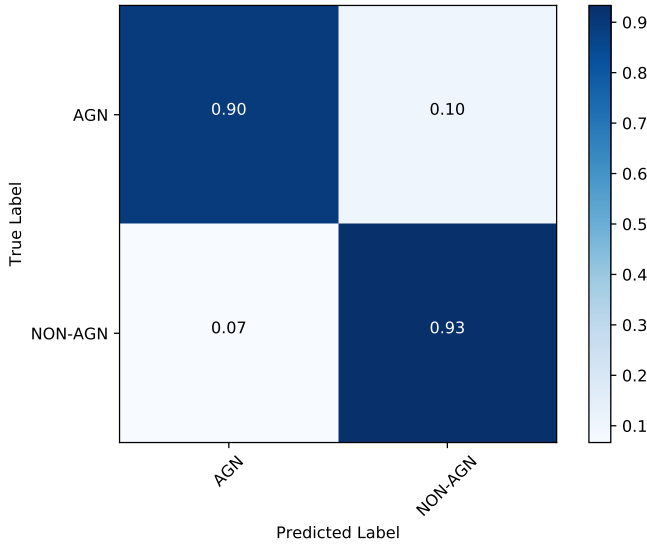


Figure 3. Confusion matrix from testing the RF1 classifier in the test set. True Label represent the classification done from SDSS spectra, and Predicted Label is the outcome of the RF1 classifier.

We also compute the accuracy (A), precision (P), recall (R), and F1 scores, which are defined by means of the True Positives (TP: known AGN classified as AGN by the RF classifier), the False Positives (FP: known stars classified as AGN), the True Negatives (TN: known

stars classified as stars), and the False Negatives (FN: known AGN classified as stars):

$$\begin{aligned}
 A &= \frac{TP + TN}{Total\ Sample} \\
 P &= \frac{TP}{TP + FP} \\
 R &= \frac{TP}{TP + FN} \\
 F1 &= 2 \times \frac{P \times R}{P + R}
 \end{aligned} \tag{1}$$

Table 3 shows the calculated scores. for the RF1 classifier. From these scores, and from the confusion matrix, we can say that RF1 presents a low fraction of False Positives, thus, the sample of predicted AGN has a low contamination of stars. However, we tend to miss a fraction of real AGN ($\sim 10\%$). This is produced by the difficulty of detect a variable signal from AGN with low variability, and since we are only considering variability properties for the classification, they can be classified as stars.

It is important to consider that we are testing the RF1 classifier in a sample of AGN selected mostly by means of their optical colors, and since we are only considering variability features in our selection, the confusion matrix and the different scores, obtained from our labeled sample, will not be a good prediction of the performance of our method in the unlabeled sample.

One of the advantages of the RF classification is that we can easily know the feature importance, since it provides a ranking score for each feature, which tell us how well every feature separate the two classes. In the firsts columns of Table 4 we provide the list of features, ordered by importance (according to the rank value), for the RF1 classifier. It can be seen that the four most important features are the amplitude of the structure

Table 3. Scores measured in the test set for each classifier

Score	RF1	RF2
Accuracy	0.916	0.923
Precision	0.909	0.909
Recall	0.933	0.950
F1	0.921	0.930

Table 4. Feature importance for each classifier.

RF1		RF2	
Feature	Rank	Feature	Rank
A_{SF}	0.197	A_{SF}	0.209
σ_{rms}	0.139	σ_{rms}	0.149
Meanvariance*	0.127	Q31*	0.102
Q31*	0.111	P_{var}	0.093
P_{var}	0.095	Std*	0.088
Std*	0.090	Meanvariance*	0.086
PercentAmp*	0.040	PercentAmp*	0.045
γ_{SF}	0.036	Autocor-length*	0.035
Autocor-length*	0.033	γ_{SF}	0.031
MedianBRP*	0.025	$r - i$	0.028
LinearTrend*	0.023	MedianBRP*	0.021
PeriodLS	0.023	PeriodLS	0.020
η^{e*}	0.023	η^{e*}	0.019
Beyond1Std*	0.019	Beyond1Std*	0.019
StetsonK*	0.018	LinearTrend*	0.019
Con*	0.002	$i - z$	0.019
		StetsonK*	0.014
		Con*	0.002

Note. (*) Features from FATS

function, the excess variance, and the Meanvariance and Q31 parameters from FATS. As an example, we show in Figure 4 the distribution of the A_{SF} and Q31 features for the labeled set. We show with black dots those AGN classified as variable, according to the definition proposed by Sánchez et al. (2017), where a source is classified as variable when its light curve satisfies $P_{var} \geq 0.95$ and $(\sigma_{rms}^2 - err(\sigma_{rms}^2)) > 0$. From the figure, it can be seen that AGN and stars are clearly separated by these two features, and also that the majority of the AGN with low amplitude of the variability are classified as non-variable.

3.4.2. Classification considering variability features and optical colors

Our second RF classifier (RF2) includes variability features and the $r - i$ and $i - z$ colors. Figure 5 shows the confusion matrix for RF2. In this case, the confu-

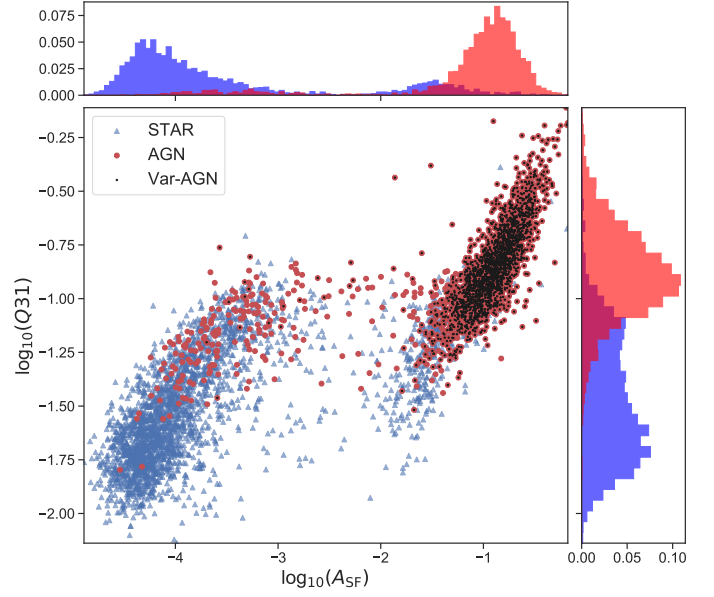


Figure 4. Distribution of the A_{SF} and Q31 features for the labeled set. Blue triangles correspond to stars, and red circles correspond to AGN. We demarc with black dots those AGN classified as variable, according to the definition used in Sánchez et al. (2017).

sion matrix is similar than the confusion matrix for RF1, however, in the case of RF2 we have a slightly purer population of AGN candidates. The accuracy, precision, recall, and F1 scores are shown in Table 3. There are not significant differences in the scores comparing with RF1.

In Table 4 we also show the ranking of features for the RF2 classifier. There are not important differences comparing with RF1. It can be seen that the variability features are in general more important than the $r - i$ and $i - z$ colors for the classification. In this case, the most important features are A_{SF} , σ_{rms} , Q31*, and P_{var} . We can also see that $r - i$ is more important than $i - z$ to classify our sources.

3.5. AGN candidates from QUEST-La Silla

We applied the trained RF1 and RF2 classifiers to our unlabeled well sampled set of 208,583 light curves. In order to improve the purity of our selection, we considered the predicted class probability (P_{RF}) to select the final set of AGN candidates. We defined two samples of AGN candidates: a) a sample with all those sources classified as AGN by the RF classifier (the full-AGN sample), and b) a sample with all those sources classified as AGN by the RF classifier, with a high probability, i.e. with $P_{RF} \geq 0.8$ (the hp-AGN sample). In Table 5 we provide a summary with the number of sources classified as AGN in both samples, for the classifiers RF1 and

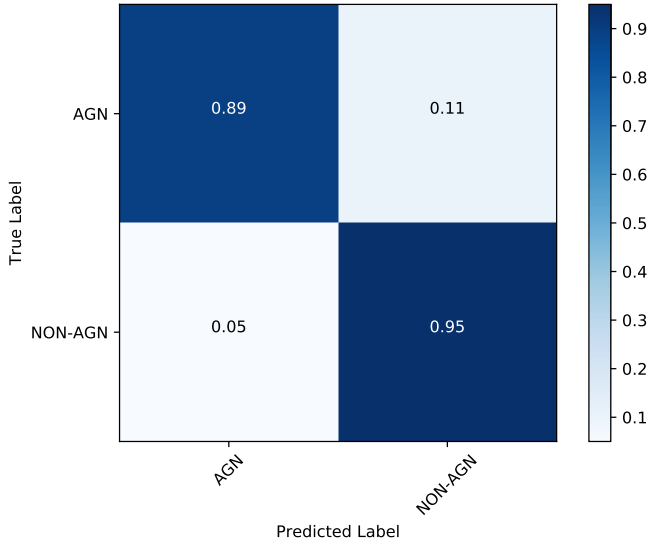


Figure 5. Confusion matrix from testing the RF2 classifier in the test set. True Label represent the classification done from SDSS spectra, and Predicted Label is the outcome of the RF2 classifier.

Table 5. Number of AGN candidates per field, for each classifier

Field	RF1		RF2	
	full-AGN	hp-AGN	full-AGN	hp-AGN
COSMOS	3,968	1,503	3,562	1,201
XMM-LSS	6,441	2,374	5,774	2,106
Elais-S1	3,374	988	2,936	942
ECDF-S	3,337	1,076	2,828	1,003
Total	17,120	5,941	15,100	5,252

RF2. For the case of the RF1 classifier, there are 17,120 sources in the full-AGN sample, and 5,941 sources in the hp-AGN sample. For the case of the RF2 classifier there are 15,100 sources in the full-AGN sample, and 5,252 sources in the hp-AGN sample. There are 4,890 candidates in common between the RF1 and RF2 hp-AGN samples. For the rest of the analysis we only considered the hp-AGN samples of RF1 and RF2.

Figure 6 shows the $r-i$ vs $i-z$ distribution of the unlabeled set, and the hp-AGN samples for the RF1 and RF2 classifiers. Comparing with Figure 2, we can see that several of our AGN candidates are located in regions of the color-color space where AGN are not normally found, particularly for the case of RF1. As expected, the main difference between the candidates of RF1 and RF2, is the exclusion of sources in the color-

color region where we normally find cold stars, for the case of RF2.

We did a visual inspection of the RF1 hp-AGN candidates, located in different areas of the color-color diagram, particularly in those areas where AGN are not normally found, like in the stellar locus. In Figure 6 we show the position in the $r-i$ vs $i-z$ diagram of some of these candidates. Four of these candidates are not present in the RF2 hp-AGN sample. As an example, we marked with letters (ABCD) four candidates located in different positions of the stellar locus, and in Figure 8 we show their light curves. From the figure, it can be seen that their are highly variable.

4. CONFIRMATION OF AGN CANDIDATES

The fields considered in this work were selected because they are some the most intensively observed regions in the southern sky, with a huge amount of ancillary data ranging from X-rays to radio waves, which can be extremely useful to confirm the nature of some of our candidates.

In the following sections, we show the results on confirming the nature of some of our candidates by using ancillary data. We also show the results of a spectroscopic follow up campaign executed between December 2016 and September 2018, done to test the efficiency of our selection method.

In particular, we were interested in confirm the nature of sources located in positions of the color-color space where AGN are not normally found (e.g. in the stellar locus). We divided our high probability candidates samples according to their $g-r$ colors (we avoid $u-g$ since u is not available for some of our fields). We define the blue sample as the one composed by sources with $g-r \leq 0.6$ and the red sample as the one composed by sources with $g-r > 0.6$. As can be seen in Figure 2 most of the AGN in the labeled set have $g-r \leq 0.6$.

4.1. Confirmation by ancillary data

The Million Quasars Catalog (MILLIQUAS v5.7 update, Flesch 2015) provides a very complete compendium of know AGN (both type 1 and type 2), from the literature, including the last data release of SDSS. It also include a list of high-confidence AGN candidates, from different sources like AllWISE (Secrest et al. 2015).

We used the MILLIQUAS to confirm the nature of our candidates. In Table 6 we show the number of candidates confirmed using this catalog, dividing the hp-AGN sample in red and blue samples. It can be seen that most of the confirmed sources are in the blue sample ($\sim 61\%$ for each classifier). Less than the 10% of the confirmed sources have $g-r > 0.6$. There are 354 and

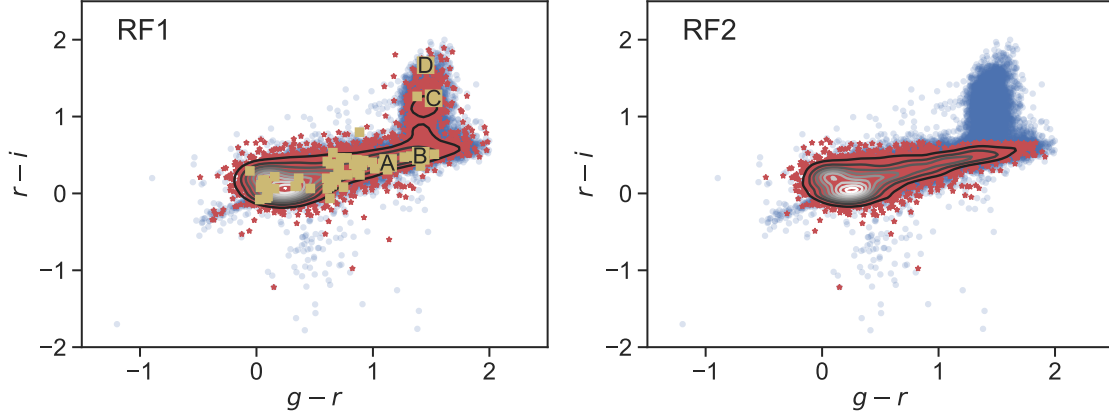


Figure 6. $r-i$ vs $i-z$ diagrams of the unlabeled set (blue circles), and the hp-AGN sample (red stars). In the left panel we show the candidates for the RF 1 classifier, and in the right panel for the RF2 classifier. The contour plots show the distribution of the hp-AGN samples for RF1 and RF2. In the left pane, we mark with yellow squares the position of candidates observed during a spectroscopic follow up campaign, and with larger yellow squares and letters the position of a selection of observed candidates located in the stellar locus.

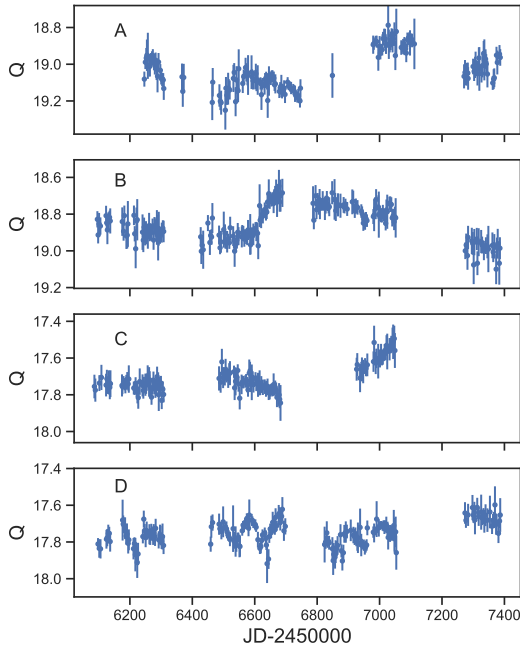


Figure 7. Light curves of some RF1 candidates located in the stellar locus, shown in Fig. 6.

356 AGN candidates for RF1 and RF2 classifiers respectively, classified as AGN candidates by MILLIQUAS. Most of them are candidates from WISE (Secretst et al. 2015).

4.2. Spectroscopic follow up of AGN candidates

Since most of the AGN confirmed by using ancillary data have blue colors ($g-r \leq 0.6$), we performed a spectroscopic follow up to confirm the nature of sources located in different regions of the color-color space. We used the SOAR/Goodman (Clemens et al. 2004) and the NTT/EFOSC2 (Buzzoni et al. 1984) instruments to observe 54 candidates from both RF1 and RF2 samples. There are 50 sources that belong to RF1 and RF2 samples, and 4 that belong only to RF1. The candidates were selected by visual inspection of the light curves of candidates located in different positions of the $g-r$ vs $r-i$ space. In Figure 6 we show the color distribution of the observed candidates with yellow squares. The full list of observed candidates can be found in Section A of the appendix.

A 70% of the observed candidates (38 targets) have $g-r > 0.6$. We used the obtained spectra to classify our targets and to estimate their redshifts. In Table 7 we provide a summary of the follow up campaign. We divided the sources in the blue and red samples, and we also separate the sources according to their spectroscopic classes: QSO1 (type 1 QSO), Seyfert 1, BAL-QSO, galaxy, and star. In Table 7 of the appendix we present the results of our follow up campaign. We provide the position of the observed sources, their redshift, their $g-r$ color, and their spectroscopic classification.

As can be seeing in Table 7, most of the blue candidates observed are classified as QSO1, on the other hand, the population of observed sources with $g-r > 0.6$ is more varied. Besides, the efficiency ($\text{confirmed AGN} / \text{AGN candidates}$) is 100% for the blue sample (for both classifiers), and for the case of the red sample the efficiency is 73.7% and 80% for RF1 and

Table 6. Number of AGN candidates confirmed using MILLIQUAS, for each classifier

Sample	RF1		RF2	
	MILLIQUAS AGN	hp-AGN	MILLIQUAS AGN	hp-AGN
blue	2,206	3,618	2,216	3,613
red	152	2,323	150	1,639

Table 7. Summary of the spectroscopic follow up campaign

Class	blue sample	red sample	Total
QSO1	15	12	27
Seyfert1	0	11	11
BAL-QSO	1	5	6
Galaxy	0	5	5
Star	0	5	5

RF2 respectively. For the case of the whole sample, we achieve an efficiency of 81.5% for the RF1 classifier, and 86.3% for the RF2 classifier.

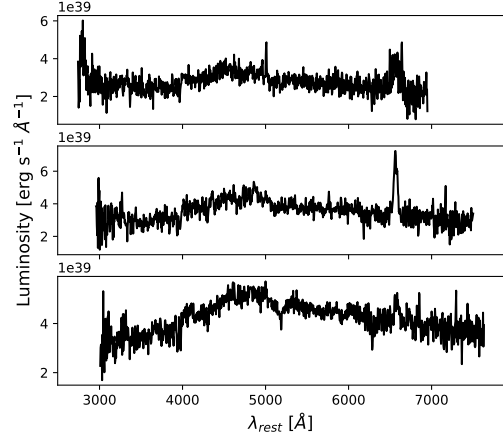
In Figure 6 we show the distribution of the observed sources in the $g-r$ vs $r-i$ space, and we mark with letters some candidates located in the stellar locus. The sources A and B are classified as Seyfert1, and the sources C and D are classified as type M stars. From the light curves of the sources C and D (see Figure 8) and from their spectra, we propose that these candidates are long period variable stars (LPV).

There are 5 targets with redshift higher than 2.5. These type of sources are very hard to detect using typical color-color selections (Palanque-Delabrouille et al. 2011; Butler & Bloom 2011). Besides, there are 6 sources with clear broad absorption lines, with 5 of them having $g-r > 0.6$. Moreover, there are 22 AGN with $z_{spec} < 0.7$, with 20 of them having $g-r > 0.6$, and 8 of these are LLAGN, whose continuum are significantly dominated by the host galaxy, but with clear presence of their emission lines. As an example, in Figure 8 we show the spectra of three LLAGN sources.

4.2.1. Non-AGN observed candidates

We observed 10 sources classified as stars or galaxies, all these sources have clear evidence of variability. When we only consider candidates from the RF2 sample, three of the observed stars are excluded, but the galaxies are still present.

For the case of the galaxies, the light curves show clear signs of AGN-like variability. The obtained spectra of these sources are noisy (signal to noise less than 10), so probably we are missing the detection of some very faint lines. Therefore, in order to confirm the nature of

**Figure 8.** Spectra of three sources with evidence of red continuum, observed with NTT/EFOSC2.

these sources we need observations with 8-meter class telescopes.

For the case of the stars, four of them are M stars, and one seems to be a K star. We propose that these stars belong to the LPV class. From their light curves, we can conclude that they are semi-periodic variable stars. The three targets observed in the region dominated by cold stars ($g-r \sim 1.5$ and $r-i \gtrsim 0.8$), are type M stars. From these, we conclude that most of the candidates from the RF1 sample, in this region of the $g-r$ vs $r-i$ space, are variable stars, and that they probably are LPV or binary stars.

From these results, we can conclude that the best classifier is the RF2, since it is the one with the lowest fraction of contaminants, the one that avoids the region occupied mostly by cold stars, and the one with the highest efficiency.

5. COMPARISON WITH PREVIOUS WORKS

Butler & Bloom (2011) used SDSS photometry to select AGN candidates through variability in the Stripe 82 field. They used damped random walk modelling (Kelly et al. 2009) to detect quasar-like variable sources. The light curves used in their analysis have in average 10 epochs, with a maximum of 28, obtained over ~ 6 years (Sesar et al. 2007). As can be seen in Figure 8 of But-

ler & Bloom (2011), most of their candidates lie in the region where typical AGN are found, and only a $\sim 1\%$ of their candidates lie in the color-color space dominated by stars (stellar locus).

Palanque-Delabrouille et al. (2011) also use SDSS photometry to select AGN candidates through variability in the Stripe 82 field. In average, the light curves used by them have 53 ± 20 epochs, and a total coverage between 4 and 10 years. They characterized the variability of each source using the structure function, and they classified the sources using a neural network algorithm. They applied their variability selection method to select candidates to be observed during the eBOSS survey. They demonstrated that their method is very efficient selecting sources with $z_{spec} > 2.2$ and BAL-QSO. However, the fraction of candidates with stellar-like colors is low (as can be seeing in their Figure 18).

More recently, Tie et al. (2017) combined colors and variability properties to select AGN candidates from DES. They obtained light curves from the first year of DES, which span less than a year and typically have ~ 15 epochs. They used the chi-squared integrated probability to select AGN candidates. Since they have light curves with only a year of coverage, they did not implemented more sophisticated variability selection methods. They demonstrated that combining variability with optical and infrared photometry improves the efficiency of AGN selection. Tie et al. (2017) provide a catalog of 1,263 spectroscopically confirmed quasars in the DES supernova fields brighter than $i = 22$ mag. Only a 6% of their confirmed candidates have $g - r > 0.6$.

The light curves used in our analysis have a considerably better cadence than the ones used in previous variability analyses, with an average of 120 ± 48 epochs and a total length of 1306 ± 254 days. In our case a 39,1% and a 31,2% of the candidates of RF1 and RF2 respectively have $g - r > 0.6$, where stars are the dominant component. As we show in Section 4.2, most of the atypical AGN observed during the spectroscopic follow up campaign lie in this region of the color-color space. We can conclude that our selection method is more sensitive to atypical AGN, like LLAGN, than previous analyses, which might be related with the higher probability to detect a variable signal from our light curves.

Our selection technique has the advantage of being easily applicable to LSST data, since the expected cadence for the DDF will be similar that the one used here (LSST Science Collaboration et al. 2009). LSST will provide multi-band light curves, which will improve the detection of false positives and the proper characterization of the variability properties of the candidates.

6. CONCLUSIONS

We have presented a methodology to classify AGN through variability analyses, particularly useful to find AGN populations missed by other optical selection techniques. We used data from the QUEST-La Silla AGN variability survey to construct a total of 208,583 well sampled light curves in the COSMOS, XMM-LSS, Elais-S1, and ECDF-S fields. We characterize the variability of these sources by using different variability features (see Section 3.2). We used a Random Forest algorithm to classify our objects as either AGN or non-AGN using variability features and optical colors. We tested two classification schemes, one that includes only variability features (RF1), and another one that includes variability features and some optical colors (RF2). Considering the distribution of known AGN and stars in the color-color diagrams of Figure 2, we decided to include in our classification only the $r - i$ and $i - z$ colors. We have a total of 5,941 AGN candidates for the RF1 classifier, and 5,252 candidates for the RF2 classifier.

We confirmed the nature of our candidates by using ancillary data, and we found that a high fraction of our candidates with $g - r \leq 0.6$ are known AGN from the literature (see Section 4.1). Less than the 10% of confirmed candidates have $g - r > 0$. This motivated us to perform a spectroscopic follow up campaign (see Section 4.2), in order to test the success of our method to classify sources with $g - r > 0$.

We observed 54 candidates with NTT/EFOSC2 and SOAR/Goodman. A 70% of the observed targets have $g - r > 0$. During the campaign, we confirm the nature of several interesting sources, like 5 BAL-QSO, 5 sources with $z_{spec} > 2.5$, and 8 LLAGN. Our method was very efficient in classifying AGN with $g - r \leq 0.6$, for which we achieved a 100% of efficiency for both classifiers. For the case of sources with $g - r > 0$, our method had also a good performance, achieving a 73.7% of efficiency for RF1 and 80% of efficiency for RF2.

From the spectroscopic follow up campaign, we can conclude that the best classifier is the one that includes variability features and the $r - i$ and $i - z$ colors (RF2). Since it avoids the region of the color-color space where we normally find cold stars, and also because it showed the highest efficiency. For the case of RF1, we propose that most of the candidates with $g - r \sim 1.5$ and $r - i \gtrsim 0.8$ are LPV or binary stars.

Our work can be considered as a pilot study in preparation for LSST, since the selection techniques tested here can be easily implemented for LSST data. The cadence of the LSST's DDF will be similar that the one of QUEST-La Silla, but covering 10 years of observations,

which will improve considerably the selection efficiency. Besides, LSST will provide observations in more than one photometric band, which will be extremely useful to discard artefacts and false positives.

PS was supported by CONICYT through Beca Doctorado Nacional, Año 2013 grant #21130441. PS received partial support from Center of Excellence in Astrophysics and Associated Technologies (PFB 06). PL acknowledges Fondecyt Grant #1161184.

This work is based on observations obtained at the Southern Astrophysical Research (SOAR) telescope, which is a joint project of the Ministério da Ciência, Tecnologia, Inovações e Comunicações (MCTIC) do Brasil, the U.S. National Optical Astronomy Observatory (NOAO), the University of North Carolina at Chapel Hill (UNC), and Michigan State University (MSU).

Funding for the SDSS and SDSS-II has been provided by the Alfred P. Sloan Foundation, the Participating Institutions, the National Science Foundation, the U.S. Department of Energy, the National Aeronau-

tics and Space Administration, the Japanese Monbukagakusho, the Max Planck Society, and the Higher Education Funding Council for England. The SDSS Web Site is <http://www.sdss.org/>.

The SDSS is managed by the Astrophysical Research Consortium for the Participating Institutions. The Participating Institutions are the American Museum of Natural History, Astrophysical Institute Potsdam, University of Basel, University of Cambridge, Case Western Reserve University, University of Chicago, Drexel University, Fermilab, the Institute for Advanced Study, the Japan Participation Group, Johns Hopkins University, the Joint Institute for Nuclear Astrophysics, the Kavli Institute for Particle Astrophysics and Cosmology, the Korean Scientist Group, the Chinese Academy of Sciences (LAMOST), Los Alamos National Laboratory, the Max-Planck-Institute for Astronomy (MPIA), the Max-Planck-Institute for Astrophysics (MPA), New Mexico State University, Ohio State University, University of Pittsburgh, University of Portsmouth, Princeton University, the United States Naval Observatory, and the University of Washington.

REFERENCES

- Abbott, T. M. C., Abdalla, F. B., Allam, S., et al. 2018, ArXiv e-prints, arXiv:1801.03181
- Abolfathi, B., Aguado, D. S., Aguilar, G., et al. 2018, *ApJS*, 235, 42
- Allevato, V., Paolillo, M., Papadakis, I., & Pinto, C. 2013, *ApJ*, 771, 9
- Antonucci, R. R. J., & Miller, J. S. 1985, *ApJ*, 297, 621
- Bertin, E., & Arnouts, S. 1996, *A&AS*, 117, 393
- Breiman, L. 2001, *Machine Learning*, 45, 5
- Butler, N. R., & Bloom, J. S. 2011, *AJ*, 141, 93
- Buzzoni, B., Delabre, B., Dekker, H., et al. 1984, *The Messenger*, 38, 9
- Cartier, R., Lira, P., Coppi, P., et al. 2015, *ApJ*, 810, 164
- Clemens, J. C., Crain, J. A., & Anderson, R. 2004, in *Proc. SPIE*, Vol. 5492, *Ground-based Instrumentation for Astronomy*, ed. A. F. M. Moorwood & M. Iye, 331–340
- Covey, K. R., Ivezić, Ž., Schlegel, D., et al. 2007, *AJ*, 134, 2398
- Doi, M., Tanaka, M., Fukugita, M., et al. 2010, *AJ*, 139, 1628
- Flesch, E. W. 2015, *PASA*, 32, e010
- Gunn, J. E., Carr, M., Rockosi, C., et al. 1998, *AJ*, 116, 3040
- Ivezic, Z., Tyson, J. A., Abel, B., et al. 2008, ArXiv e-prints, arXiv:0805.2366
- Kelly, B. C., Bechtold, J., & Siemiginowska, A. 2009, *ApJ*, 698, 895
- Kelly, B. C., Becker, A. C., Sobolewska, M., Siemiginowska, A., & Uttley, P. 2014, *ApJ*, 788, 33
- Kim, D.-W., Protopapas, P., Bailer-Jones, C. A. L., et al. 2014, *A&A*, 566, A43
- Kim, D.-W., Protopapas, P., Byun, Y.-I., et al. 2011, *ApJ*, 735, 68
- LaMassa, S. M., Cales, S., Moran, E. C., et al. 2015, *ApJ*, 800, 144
- LSST Science Collaboration, Abell, P. A., Allison, J., et al. 2009, arXiv e-prints, arXiv:0912.0201
- McLaughlin, M. A., Mattox, J. R., Cordes, J. M., & Thompson, D. J. 1996, *ApJ*, 473, 763
- Myers, A. D., Palanque-Delabrouille, N., Prakash, A., et al. 2015, *ApJS*, 221, 27
- Netzer, H. 2015, *ARA&A*, 53, 365
- Nun, I., Protopapas, P., Sim, B., et al. 2015, ArXiv e-prints, arXiv:1506.00010
- Palanque-Delabrouille, N., Yèche, C., Myers, A. D., et al. 2011, *A&A*, 530, A122
- Rahman, M., Mendez, A. J., Ménard, B., et al. 2016, *MNRAS*, 460, 163
- Richards, G. T., Fan, X., Newberg, H. J., et al. 2002, *AJ*, 123, 2945

- Richards, G. T., Myers, A. D., Gray, A. G., et al. 2009, ApJS, 180, 67
- Richards, J. W., Starr, D. L., Butler, N. R., et al. 2011, ApJ, 733, 10
- Ross, N. P., Myers, A. D., Sheldon, E. S., et al. 2012, ApJS, 199, 3
- Sánchez, P., Lira, P., Cartier, R., et al. 2017, ApJ, 849, 110
- Sánchez-Sáez, P., Lira, P., Mejía-Restrepo, J., et al. 2018, ApJ, 864, 87
- Schmidt, K. B., Marshall, P. J., Rix, H.-W., et al. 2010, ApJ, 714, 1194
- Secrest, N. J., Dudik, R. P., Dorland, B. N., et al. 2015, ApJS, 221, 12
- Sesar, B., Ivezić, Ž., Lupton, R. H., et al. 2007, AJ, 134, 2236
- Tie, S. S., Martini, P., Mudd, D., et al. 2017, AJ, 153, 107
- VanderPlas, J., Connolly, A. J., Ivezić, Z., & Gray, A. 2012, in Proceedings of Conference on Intelligent Data Understanding (CIDU), pp. 47-54, 2012., 47–54
- VanderPlas, J. T. 2018, ApJS, 236, 16
- York, D. G., Adelman, J., Anderson, Jr., J. E., et al. 2000, AJ, 120, 1579

APPENDIX

A. CATALOG OF OBSERVED CANDIDATES

Here we present the list of candidates observed during our spectroscopic follow up campaign. We provide the position, the telescope used, the measured redshift, a flag with the quality of the measured redshift (0: no redshift available, 1: low quality z_{spec} , 2: good quality z_{spec}), the $g - r$ color, and the spectroscopic classification.

Table 8. Targests observed during spectroscopic follow up.

Name	RA	DEC	Telescope	z_{spec}	FLAG $_{z_{spec}}$	$g - r$	Class
QLS_1	7.021016	-45.806145	SOAR	3.5852	1	1.13	QSO1
QLS_2	7.263506	-45.629417	NTT	1.3796	2	0.63	QSO1
QLS_3	7.323368	-43.633305	SOAR	0.3242	1	0.03	QSO1
QLS_4	7.377026	-46.529945	NTT	0.2824	1	1.53	Gal
QLS_5	7.387083	-43.664276	NTT	0.2000	1	1.08	Gal
QLS_6	7.418616	-42.320072	NTT	0.0000	2	1.52	STAR
QLS_7	7.419530	-43.789948	NTT	0.3912	2	1.12	Seyfert1
QLS_8	7.820146	-45.645706	NTT	0.3123	2	1.41	Seyfert1
QLS_9	7.970508	-42.275764	NTT	0.1847	2	0.99	Seyfert1
QLS_10	8.304768	-45.681595	NTT	0.2676	2	0.92	Seyfert1
QLS_11	8.348364	-46.856922	NTT	3.5297	2	0.75	QSO1
QLS_12	8.629325	-42.310108	SOAR	-99.0000	0	1.38	STAR
QLS_13	8.787973	-45.348194	NTT	0.1469	2	0.64	Seyfert1
QLS_14	9.407302	-43.000004	NTT	2.0000	1	0.69	BAL-QSO
QLS_15	9.414984	-43.422619	SOAR	1.8265	2	-0.06	QSO1
QLS_16	10.021671	-43.859173	NTT	0.3710	2	0.86	Seyfert1
QLS_17	10.097470	-44.866116	NTT	-99.0000	0	0.70	BAL-QSO
QLS_18	10.225745	-43.855934	NTT	1.2671	1	0.63	QSO1
QLS_19	10.758265	-42.452019	NTT	0.1000	1	0.89	Gal
QLS_20	10.866718	-43.825359	NTT	-99.0000	0	0.65	BAL-QSO
QLS_21	11.090293	-43.665966	NTT	0.0000	2	0.78	STAR
QLS_22	30.591522	-2.020991	SOAR	2.0502	2	0.04	QSO1
QLS_23	30.603312	-1.752825	NTT	0.2101	2	0.71	Seyfert1
QLS_24	31.057844	-2.953287	SOAR	0.1500	1	0.91	Gal
QLS_25	31.167528	-3.630512	NTT	-99.0000	0	0.61	BAL-QSO
QLS_26	31.533081	-2.510754	SOAR	1.4319	1	0.09	QSO1
QLS_27	32.158398	-3.652800	NTT	0.0000	2	1.45	STAR
QLS_28	32.456287	-3.651828	SOAR	1.4976	2	0.09	QSO1
QLS_29	33.409081	-3.250347	SOAR	2.8491	2	0.16	QSO1
QLS_30	33.474072	-3.279924	NTT	0.5671	1	0.88	QSO1
QLS_31	36.426113	-2.971209	NTT	0.0000	2	0.67	STAR
QLS_32	36.852539	-2.401858	NTT	0.2551	2	0.84	QSO1
QLS_33	37.988422	-2.585521	SOAR	0.3498	2	0.09	QSO1
QLS_34	38.680885	-2.637419	SOAR	0.8437	2	0.46	QSO1
QLS_35	51.529488	-29.656691	NTT	0.2307	2	0.87	Seyfert1
QLS_36	51.765114	-27.740358	SOAR	2.0279	2	0.07	QSO1
QLS_37	52.009411	-28.600405	NTT	0.2667	2	1.33	Gal
QLS_38	52.013538	-30.619936	NTT	0.3284	2	0.90	Seyfert1
QLS_39	52.397503	-27.657492	NTT	1.4175	2	0.60	QSO1

Continued on next page

Table 8 – *Continued from previous page*

Name	RA	DEC	Telescope	z_{spec}	FLAG	z_{spec}	$g - r$	Class
QLS_40	52.536362	-29.822481	NTT	0.1804	2		0.66	QSO1
QLS_41	52.593563	-29.353525	NTT	0.2177	2		0.61	Seyfert1
QLS_42	53.317341	-29.488207	SOAR	1.9234	2		0.16	QSO1
QLS_43	53.730831	-27.736212	NTT	2.6249	1		0.86	BAL-QSO
QLS_44	53.749317	-27.499168	NTT	0.3598	2		1.13	Seyfert1
QLS_45	53.847992	-28.123224	SOAR	0.8682	2		0.09	QSO1
QLS_46	53.864979	-26.950115	SOAR	0.8159	2		0.04	QSO1
QLS_47	53.911106	-28.961195	NTT	0.2116	2		0.72	QSO1
QLS_48	53.943211	-27.432163	NTT	0.4332	1		1.02	QSO1
QLS_49	54.049484	-28.095388	SOAR	2.5265	2		0.10	QSO1
QLS_50	54.782047	-26.617104	SOAR	0.3825	2		0.70	QSO1
QLS_51	54.785744	-28.131121	SOAR	2.1388	1		0.34	BAL-QSO
QLS_52	54.878654	-27.307127	SOAR	1.0899	2		0.62	QSO1
QLS_53	55.059608	-26.485237	SOAR	1.6453	2		0.05	QSO1
QLS_54	149.004532	1.161204	SOAR	2.3530	1		0.33	QSO1